RESEARCH ARTICLE

WILEY

Aerodynamics of an airfoil with leading-edge icing

Magnus K. Vinnes 🟢 ｜ R. Jason Hearst 🟢

Department of Energy and Process Engineering, Norwegian University of Science and Technology, Trondheim, Norway

Correspondence
R. Jason Hearst, Department of Energy and Process Engineering, Norwegian University of Science and Technology, Trondheim 7041, Norway.
Email: jason.hearst@ntnu.no

Abstract

The flow over the leading edge of an NREL S826 reference airfoil with three different icing-inspired leading-edge contamination geometries has been assessed experimentally. Particle image velocimetry was performed on the leading edge of the airfoil for a range of angles-of-attack between $-4°$ and $16°$. This work primarily focuses on the flow physics at Reynolds numbers (Re_c = 455 000) within the Reynolds number independent regime of the airfoil. The present work illuminates our understanding of the flow phenomena as well as provides a validation dataset for future numerical work. From the acquired data, the mean velocity, turbulent kinetic energy and mean vorticity have been estimated. The results show how the different contamination geometries affect the point of separation. It is also shown that the intermittency of the flow behind horn-shaped contamination is dependent on the angle-of-attack, even at angles above stall. Proper orthogonal decomposition was performed on the velocity fields to identify whether reduced order modelling is an appropriate tool for rapid estimation of these flows. It was found that a limited number of modes carried a large fraction of the fluctuating energy, demonstrating that reduced order modelling is feasible.

KEYWORDS
airfoil, contamination, flow, icing, turbulence

1 ｜ INTRODUCTION

Leading-edge contamination is a problem that plagues airfoils in a variety of settings and applications, one of which is wind energy. The global wind energy industry is expanding, with over 50-GW added capacity installed yearly between 2014 and 2018.[1] Some attractive wind farm locations, in terms of wind resources, have undesirable side effects for the turbines, for example, leading-edge fouling on the wind turbine blades. Insects thrive in warm, humid climates, and when they impact turbine blades, it can lead to contamination. The same effect can occur in environments with dust or dirt particles in the air. Such particles can lead to erosion near the leading edge. In cold climates, atmospheric icing conditions lead to ice accretions building up around the leading edge of the airfoil.

Contamination on the wind turbine airfoils reduces the energy production of the turbine. Several recent studies show that the annual energy production (AEP) is reduced by dust contamination; for example, Han et al.[2] found that the AEP was reduced by 2–3.7% by contamination and erosion, while Dollinger et al.[3] found an AEP reduction of 4.7%. Ice accretions can lead to even larger reductions in AEP; for example, icing on the airfoils led to AEP reductions of 12% and 19% for a full scale three bladed turbine at the Acqua Spruzza test cite in central Italy.[4] To maintain the rotation of a vertical axis rotating rig, Han et al.[5] found that the torque requirement increased 70% under severe icing conditions. Recently, Yirtici et al.[6] predicted 17% power loss for a NREL 5-MW wind turbine during icing conditions. In addition, icing on the airfoil leads to

measurement errors due to ice accretion on sensors and increased mechanical loads, which can ultimately lead to mechanical failures, electrical failures, changes in material properties and safety issues related to ice being thrown from the rotor blades.[7] The severity of these issues clearly identifies turbine blade contamination as a key problem in wind energy.

Focusing on classifying the types of blade contamination, Bragg et al.[8] distinguished ice accretions by their geometry, in contrast to traditional classification based on the atmospheric conditions (e.g., used by Han et al.[5]). This is useful when the aerodynamic performance of the airfoil is assessed. Since these classifications are based on the geometry of the accretions, the same classification can be used for other leading edge contamination. Bragg et al.[8] used the term *roughness* to describe small ice particles at the leading edge that change surface texture but could also be used to describe sand grains embedded in the blade for instance. The roughness height is usually larger than the local boundary layer thickness. *Horn ice* features one or two horn shapes that protrude from the leading edge. This geometry often has significant impact on the aerodynamic performance of the airfoil. *Streamwise* icing geometries are more aerodynamically shaped. They consist of a layer of ice around the leading edge. In some cases, streamwise ice might grow into a horn protruding straight from the leading edge. The last geometry, *streamwise-ridge* icing, happens downstream of the leading edge and appears like feathers from the airfoil. Typically, water droplets travel from the leading edge, where heating elements are installed on planes for instance, and freeze when they reach the end of the heating element. During some icing conditions, experimental results show possible generation of ice feathers or rivulets downstream of the leading edge.[9] These are not necessarily seen in simulations.[10]

Regardless of the categorisation methodology, the various types of contamination affect the flow field differently. The most extreme cases have horn like geometries.[5] For such cases, the geometry of the contamination determines the flow, and separation is typically located at the tip of the horn for all angles-of-attack (α). This generally leads to thin airfoil type stall,[11] characterised by a separation bubble starting at the leading edge, which expands with increasing α until the flow is unable to reattach.[12-14] The surface roughness of the contamination has a larger effect on the flow for streamlined ice accretions. The roughness mostly affects the drag but also moves the point of turbulent transition farther upstream, due to increased turbulence production near the leading edge.[11] This is typical behaviour for trailing edge stall, where the separation point moves from the trailing edge towards the leading edge with increasing α.[12-14]

Several experiments have been performed to measure the forces acting on an airfoil subjected to icing.[10,15-20] The pressure distribution of the flow has also been evaluated for various icing geometries.[18,20,21] Increased drag and reduced lift are observed in most studies. The magnitude of these parameters is dependent on the geometry of the icing profile, the airfoil, the Reynolds number (Re), α, and icing conditions. Blasco et al.[17] found that drag increase varies with the surface roughness of the icing, while the lift reduction varies with the impingement length of the icing geometry. Hann et al.[20] investigated a NREL S826 airfoil with different icing-inspired leading-edge contaminations. They measured drag and lift at $Re_c = U_\infty c/\nu = 4 \times 10^5$ (where U_∞ is the incoming velocity, c is the airfoil chord length and ν is the kinematic viscosity of the fluid) and found that the lift was reduced and drag increased for all contamination geometries. Vinnes et al.[22] presented the experimentally obtained flow fields for some of these cases but did not investigate the results in significant detail. Xiao et al.[23] used large-eddy simulations (LES) on two different airfoils, with different icing geometries at the leading edge of the airfoil. In both their cases, ice accretion around the leading edge reduced the stall angle, α_{stall}. Gao et al.[19] also report reduced α_{stall} for a horn ice geometry.

According to Etemaddar et al.,[16] the increase in drag is higher than the reduction in lift for streamlined ice accretions, so the reduced performance of wind turbines is mostly due to increased drag on the airfoil. This agrees with the results from Hann et al.[20] The relative difference is smaller for high α, where the reduction in lift is more prominent.[16] Some studies report increased lift of the airfoil for some icing geometries at high α.[5,24,25] It has been suggested that in such cases, the icing acts as a leading edge slat.[5,25]

Ice contamination is a highly three-dimensional phenomena.[9,26] The increase in drag is higher when three-dimensional icing is investigated.[10] This is explained by the vortices induced in more than one plane. With a three-dimensional ice structure, the flow will be divided into cells in the spanwise direction.[27,28] Inside each cell, the flow is roughly two dimensional.[27,28] When seen from above, the flow inside a cell might have an angle compared to the incoming velocity.[27,28] Still, the separation bubble behaves in the same manner inside the cells as it would for a two-dimensional ice accretion. At the interface between the cells, the reattachment point moves farther upstream, and the height of the separation bubble is reduced.[27,28] In this region, the flow is observed to be three dimensional in nature.[27,28] Nevertheless, because the flow is two dimensional in each cell, a two-dimensional icing profile can provide insight on the mechanics of an iced airfoil. Moreover, as a real turbine blade is made-up of continuously changing cross-sections, but lab-scale measurements are typically performed in a plane on a single extruded airfoil from one of these sections, it makes sense to also extrude the icing in the same 2-D fashion. This gives us insight into the mechanics at this particular section of the blade.

Jacobs and Bragg[27,28] performed particle image velocimetry (PIV) investigations on a NACA0012 airfoil with horn ice accretion, at Re of about 9.0×10^5 and α ranging from $0°$ to $5°$. They focused on the separation bubble and reattachment length. Their experiments found two counter rotating recirculating zones, one small close to the horn ice geometry and a large main recirculation zone. The shear layer between the separation bubble and the freestream flow was also described. It is thin close to the ice horn and thickens toward the reattachment point.[27,28] The reattachment point of a separation bubble is unstable,[29-31] which explains the wide region of shear stress close to the airfoil. Similar descriptions of separation bubbles were also reported by Xiao et al.,[23] based on their LES. It has also been reported that the flow inside the separation bubble is dominated by vorticity.[21,23,32]

There is increasing interest in using reduced order modelling (ROM) to predict unsteady flow fields. The overall goal of using ROM to model flow fields is to reduce the need for computationally heavy simulations. The complex flow around a wind turbine or a wind farm covers many different scales of motion and time, which makes LES expensive and Reynolds averaged Navier–Stokes methods (RANS) inaccurate. ROM is therefore an attractive tool to model such flows (e.g., Siddiqui et al.[33]). Several recent studies used proper orthogonal decomposition (POD) as a tool to perform ROM on flow around airfoils. POD can also be used to improve our understanding of coherent motions in flow fields. Examples of flows investigated include the laminar separation bubble on the suction side of an airfoil,[34] airfoils in the deep stall regime,[35] airfoils experiencing unsteady incoming flow[36] and airfoils with leading-edge protuberances,[37] among others. However, the applicability of POD to model the flow over airfoils with leading-edge contamination, covering a large range of α and different geometries have not been described in the literature.

Previous studies focusing on flow measurements over contaminated airfoils were, with some recent exceptions, related to aircraft airfoils or symmetric airfoils. They have also mostly been performed for a limited range of α, and most studies only looked at one contamination geometry. Therefore, the aim of this work is to investigate the flow over an airfoil designed for wind turbines, with different contamination profiles attached to the leading edge. In particular, the present study investigates a clean NREL S826 airfoil and the same airfoil with three 2-D leading-edge contamination geometries. Measurements were performed with planar PIV because it provides adequate spatial resolution to capture the large scale phenomena, and it enables observation of instantaneous flow fields. Flow field comparisons are made for $-4° \leq \alpha \leq 16°$. This is followed by commentary on the vorticity in the flow. The applicability of POD for ROM of the flow over airfoils with leading edge contamination is also discussed. All results are compared to the force measurements of Krøgenes and Brandrud[18] and Hann et al.[20] who used the same set-up. In addition to enabling a comprehensive understanding of the flow phenomena around the leading edge of a contaminated airfoil, the present data set also offers a point of comparison for future numerical modellers who seek a reference database for their simulations. Simulating the flow around a contaminated airfoil is notoriously difficult given the multiscale effects on the developing boundary layer; the flow immediately adjacent to the airfoil is itself modelled in all computational fluid dynamics except for direct numerical simulations, which are too expensive for such problems.[20,23]

2 | EXPERIMENTAL PROCEDURE

2.1 | Experimental set-up

The airfoil used in the present experiments is an NREL S826, which is a reference airfoil designed for use on the blades of horizontal axis wind turbines with a diameter between 20 and 40 m. The profile is designed to give high maximum lift coefficients, low profile-drag coefficients, and little sensitivity to leading-edge roughness for $Re_c \sim 1.5 \times 10^6$.[38] The lift and drag, as well as the surface pressure distribution of the airfoil, have been characterised experimentally for Re_c on the order of 10^5.[18,20,39,40] The parameters have been shown to be Re-independent for $Re_c > 4.0 \times 10^5$.[41]

The closed-loop low-speed wind tunnel at the Norwegian University of Science and Technology (NTNU) was employed for this experimental campaign. The test section in the wind tunnel is 11.15 m long and has a cross-section of 1.80×2.71 m (height × width) at the inlet. The height of the test section increases to 1.85 m at the outlet to compensate for boundary layer growth. The background turbulence intensity for the tests was approximately 0.3%. The blocked area of the test section varied with α; however, the blockage was 5% in the worst case, and thus, no blockage correction was applied to the results. The airfoil was mounted vertically in the wind tunnel, on a rotating force balance, which allowed for changes to the α with an accuracy of ±0.25°. The chord length c of the airfoil is 0.45 m, and the airfoil spans the height of the tunnel. The design and manufacturing of the particular airfoil used in these experiments are discussed in detail in the work by Bartl et al.[41] The experiments were conducted with chord based Re_c of 4.55×10^5 (±1.5%). This Re is slightly higher than that used by Krøgenes and Brandrud,[18] who used the same set-up. However, they found only a slight Re-dependence for $2.0 \times 10^5 \leq Re_c \leq 4.0 \times 10^5$ with approximate Re-independence for higher Re. Similarly, Bartl et al.[41] found only a small Re-dependence for $2.0 \times 10^5 \leq Re_c \leq 4.0 \times 10^5$ and no dependence for $4.0 \times 10^5 \leq Re_c \leq 6.0 \times 10^5$ for the clean airfoil. Thus, the present results can be related to Krøgenes and Brandrud's[18] non-dimensional force measurements at. While some other studies[40,41] have shown unusual behaviour of this airfoil at $Re_c \leq 1.0 \times 10^5$, and some Re-dependency in post stall operating conditions at $Re_c \leq 2.0 \times 10^5$, we choose to do the present experiments in the regime that is independent of low-Re effects and thus representative of the physics encountered by the airfoil at its intended operational point, $Re_c \sim 1.5 \times 10^6$.[38]

The contamination geometries used in this study are the same as the LEWICE ice shapes used by Hann et al.[20] They were developed using the 2-D ice accretion software LEWICE,[42] which has been validated for a wide range of parameters,[43,44] and is also regularly used to generate ice contamination profiles for experiments and simulations.[5,16,25] All contaminations were developed for $\alpha = 1°$. For further information about the LEWICE input conditions and the icing-inspired geometries, see Hann et al.[20] The physical geometries were 3-D printed in PTA-plastic. In total, three geometries were investigated, with simulation input conditions corresponding to different atmospheric icing events. The contamination geometries are shown in Figure 1. The geometry of the contaminations agrees qualitatively well with ice geometries found in the literature.[6,8,15] However, ice feathers or rivulets located downstream of the leading edge are not present in the geometries used in the present study. The type C contamination geometry is horn-like. The other geometries are more streamlined, but for type B, the geometry has a horn like feature protruding
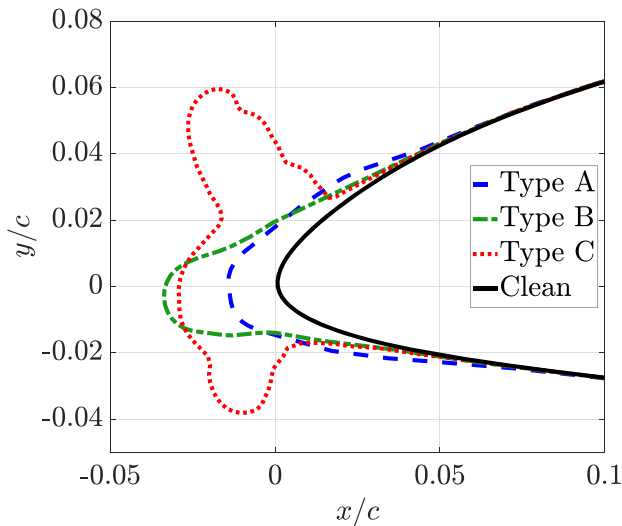
forward and appears as an extension of the chord. Note that these contamination geometries are two-dimensional, and thus represent pseudo-averages of the expected geometry along the leading-edge. Therefore, three-dimensional effects, as described by Jacobs and Bragg,[27,28] are not accounted for in the present work. However, as mentioned in the introduction, the information is useful to understand the flow inside a cell in a three-dimensional flow. For comparison, the measurements were also performed on the clean airfoil. A total of seven α were investigated for all contamination geometries and the clean case, namely, $-4°$, $0°$, $4°$, $6°$, $10°$, $14°$ and $16°$.

2.2 | Notation

In this work, the instantaneous velocity is denoted $\tilde{u}$, for the x-direction, and is defined as $\tilde{u} = U + u$, where U is the mean velocity and u is the fluctuating part. The same applies for the perpendicular velocity component, $\tilde{v}$. The total velocities are denoted by subscript tot, such that $\tilde{u}_{tot} = \sqrt{\tilde{u}^2 + \tilde{v}^2}$.

The origin of the coordinate system is at the leading edge of the airfoil, with the x-axis parallel to the chord and the y-axis perpendicular to the chord, with the positive direction towards the suction side of the airfoil. Note that this coordinate system rotates with the airfoil when α is changed. For some purposes, the wind tunnel coordinate system has been used. To distinguish the two, a superscript $*$ is added to the variable when the wind tunnel coordinate system is used. For example, the x^*-axis points in the streamwise direction of the wind tunnel. Note that the freestream velocity is always denoted as U_∞ and is measured relative to the wind tunnel frame.

To ease visualisation, masks have been applied to the figures. A light grey mask covers the airfoil itself, a medium grey mask covers the contamination geometry, and a dark grey mask covers the laser shadow. The masks are applied after processing and are not exact copies of the geometries. However, for the large field of view (FoV), the level of detail is limited, and the small extra region which might have been masked out is of limited interest.

2.3 | Data acquisition

A pitot tube was used to measure the freestream velocity U_∞. The atmospheric temperature T_{atm} was measured by a thermocouple in the wind tunnel. Both were measured at the start and end of each experimental run, and an average was used for the data acquired. Atmospheric pressure was found with a mercury barometer; at the start and the end of each day, experiments were performed; and an average was calculated for that day.

To obtain PIV image pairs, a 12-bit LaVision Imager LX 16-megapixel camera was used. A Sigma 105-mm 1:2.8D DG Macro lens was mounted to the camera. The camera was in-turn mounted in an aerodynamically profiled box beside the airfoil but still attached to the turntable. This ensured that the camera obtains the same FoV for all contamination geometries and α. Particles were illuminated with a Litron Nano L200-15, Nd-YAG dual-pulse laser, with a wavelength of 532 nm and a measured power of 208 mJ per pulse. The laser was positioned underneath the wind tunnel, and the laser pulse was redirected with mirrors before entering LaVision sheet optics. All optics were placed outside the wind tunnel, to ensure they did not disturb the flow and were not contaminated by seeding. The laser sheet entered the wind tunnel through one of the windows. Schematics of the set-up are shown in Figure 2. The FoV was limited by the size of the airfoil and the power of the laser. The range of the FoV
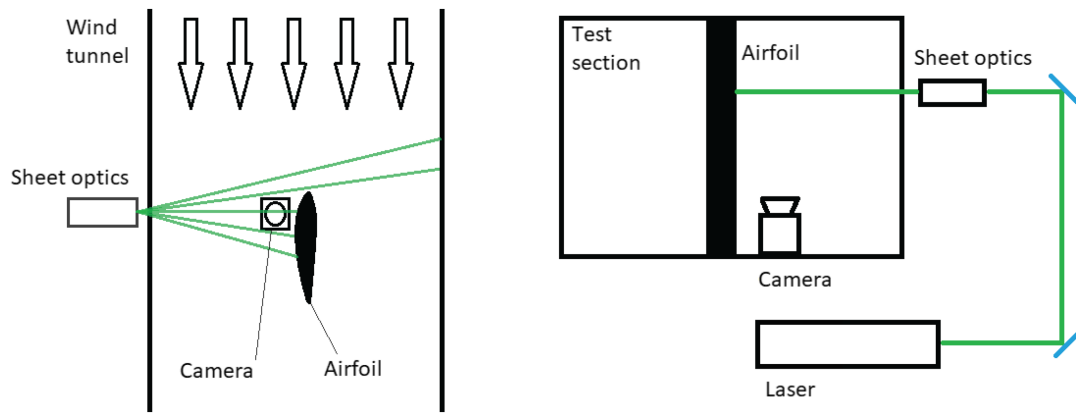
FIGURE 2 Schematics of the experimental set-up. Top view (left) and front view (right) [Colour figure can be viewed at wileyonlinelibrary. com]

was $-0.25 < x/c < 0.4$ and $-0.02 < y/c < 0.4$. Nonetheless, this is the region with the most interesting flow physics resulting from the leading-edge contamination. The particles themselves were seeded using a LeMaitre GForce 2 smoke machine. SAFEX Inside Nebelfluid Normal Power Mix and SAFEX Inside Nebelfluid Extra Clean fog fluids were used. Both are mixtures of diethylene glycol and water and give particles with a diameter of approximately 1 micron. The PIV measurement plane was approximately 1.2 m above the floor of the wind tunnel. The distance was far enough from the roof to ensure boundary layer effects were negligible. In addition, the distance from the camera to the measurement plane was sufficiently large to ensure that the box protecting the camera did not impact the flow, which was confirmed by smoke visualisations and is in agreement with the 2-dimensionality measurements performed on the same airfoil in the same wind tunnel by Bartl et al.[41]

A LaVision PTU X programmable timing unit was used to synchronise and trigger the laser and the camera. It was controlled through LaVision DaVis (version 8.4). The time step between the two frames was set to 80 μs. All data were collected with a sampling frequency of 1.63 Hz, ensuring that each vector field was statistically independent. Statistical independence between data points is important to ensure that the calculated average is a true ensemble average. For every α and for every contamination geometry, 1000 image pairs were collected, which is sufficient to converge the first- and second-order turbulent statistics in this flow.

2.4 | Processing

Processing of the data was done in LaVision DaVis (version 8.4). Preprocessing consisted of subtracting background noise from the images. First, the minimum value of every pixel over the entire data set was subtracted, followed by subtracting the minimum over a filter length of 49 images. This two-step process was used to both remove any ambient background signal as well as to account for time-varying changes in the lighting and seeding density. Processing was performed using a graphical processing unit (GPU), with a window size of 64×64 pixels and a window overlap of 50% for the first pass. The final window size was 24×24 pixels, with a window overlap of 50%, such that flow field is described by 370×239 vectors ($x \times y$). Finally, bad vectors with too high correction value were deleted, and all empty spaces were filled with vectors interpolated from the surrounding field. All further processing and calculations were made in MATLAB.

The uncertainties of the mean velocity fields were found with DaVis, which uses the correlation statistics. The specific methodology is found in previous studies.[45-47] The uncertainty is shown in Figure 3 for representative cases of attached flow, fully separated flow and partially separated flow. The maximum value of the uncertainty is approximately 3% of U_∞. Although not shown here, the uncertainty has been evaluated for all experimental cases, showing results with the same magnitudes.

3 | RESULTS

The force measurements reported by Krøgenes and Brandrud[18] and Hann et al.[20] are shown in Figure 4. For greater details on these measurements, please see the aforementioned original sources. Figure 4 shows that the type C contamination reduces α_{stall} by 5°. This agrees with results reported by DeGregorio et al.,[15] who used a NACA0012 airfoil with comparable contamination geometries. Hann et al.[20] also found that the lift, for α just below stall, decreased by 10% while drag increased from $C_d = 0.016$ to $C_d = 0.049$ at $\alpha = 0°$ for type C contamination. For the more aerodynamically shaped type A and B contaminations, lift was reduced by approximately 10%, and drag was increased by about 80% in the linear lift region. The lift reduction and drag increase were in general found to be higher for higher α.
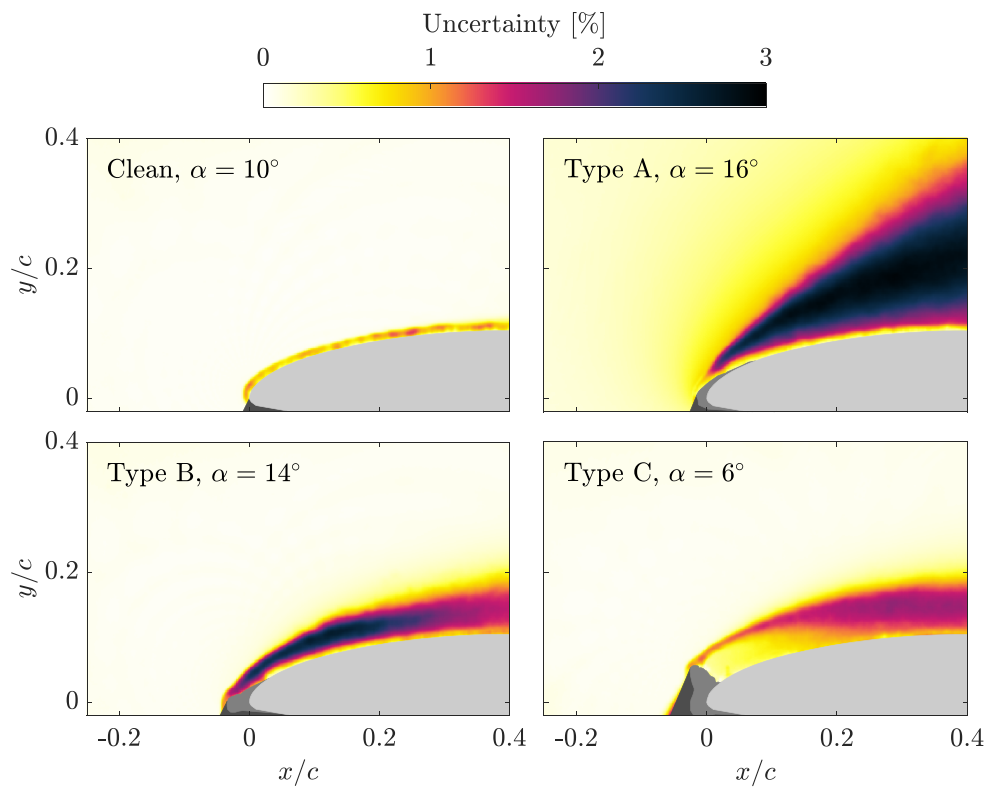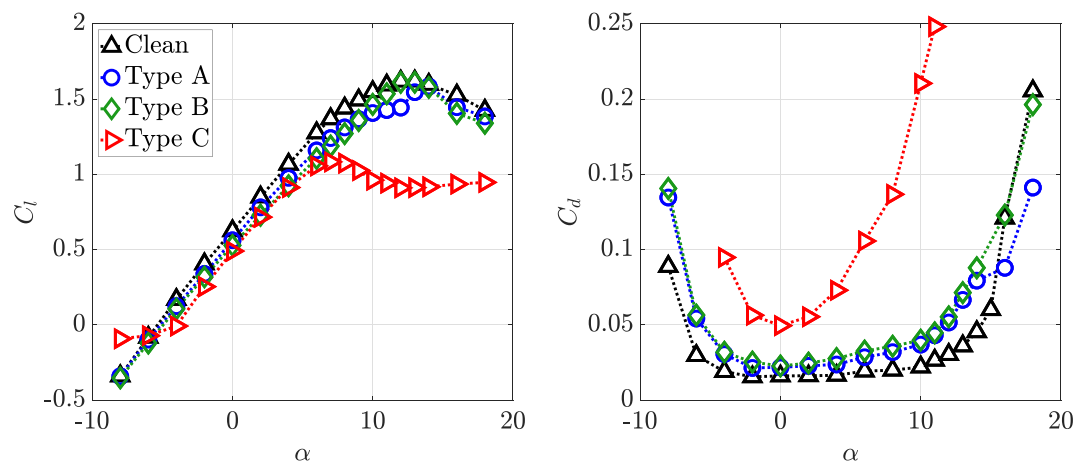
FIGURE 4 Lift (left) and drag (right) coefficients reported by Krøgenes and Brandrud[18] and Hann et al.[20] for a NREL S826 airfoil with different 2-D leading-edge contaminations [Colour figure can be viewed at wileyonlinelibrary.com]

The flow field results are presented in this section. Section 3.1 discusses the mean flow fields. Section 3.2 presents the turbulent kinetic energy (*TKE*) fields, and Section 3.3 discusses the vorticity. In each section, all contamination geometries are discussed and compared. Frequent comparison is also made to the force measurements of Hann et al.,[20] which are presented here as Figure 4.

3.1 | Mean flow

The mean flow fields are shown in Figure 5 for all contamination types and α. For the clean case at $\alpha = 16°$, the separation point is visible but not at the leading edge. Instead, the separation point is located at approximately $x/c = 0.3$. This suggests that the separation point moves from the trailing edge to the leading edge and that trailing-edge stall occurs for the clean airfoil. The trailing-edge stall behaviour is confirmed by the pressure measurements presented by Hann et al.[20] It is apparent that type A and B contamination geometries lead to separation closer to the leading edge. For type B, this is visible at $\alpha = 14°$ and is a result of a thicker boundary layer evolving from the contaminations.[8]

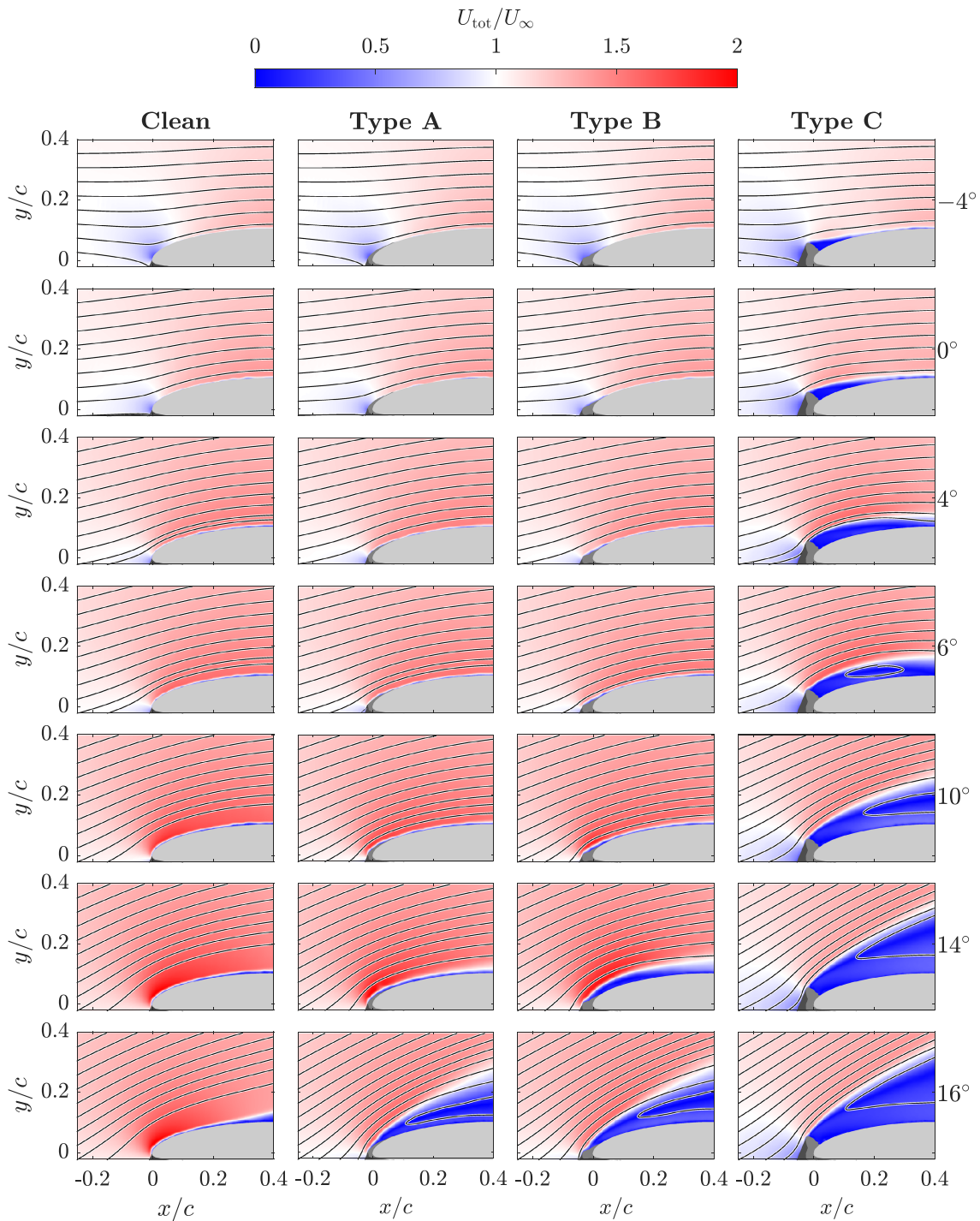$$U_{\text{tot}}/U_\infty$$

FIGURE 5 Normalised mean velocities for all experimental cases with streamlines. Please note the colourmap is centred about unity [Colour figure can be viewed at wileyonlinelibrary.com]

The shape of the C_l curves of Hann et al.[20] (Figure 4) suggests that the airfoil with type A or type B contamination experience either trailing-edge stall or thin-airfoil stall. As no separation bubble is visible in the results, it suggests trailing edge stall occurs; that is, separation starts near the trailing edge of the airfoil and moves towards the leading edge with increasing α, until stall occurs.[12] This hypothesis is supported by the pressure measurements of Hann et al.[20] that show a flat region in the C_P-curves on the suction side near the trailing edge. It also agrees with results reported by Gao et al.[19] They showed that the separation point moves toward the leading edge with increasing α. As the drag is low for the airfoil with type A contamination at $\alpha = 14°$, it is believed that flow stays attached over the airfoil. This suggests that some mechanism in the flow; for example, high turbulence production over the contamination, keeps the flow attached farther downstream on the airfoil surface than what would be expected. In Section 3.2, it will be shown that this is indeed the case.

In agreement with results observed by Han et al.[5] and Xiao et al.,[23] the separation point is always located at the horn of the type C contamination. The separation bubble increases in size for increasing α. When $\alpha \geq 6°$, it is not clear from the results if reattachment occurs for type C. This is at the end of the linear lift region and thus on the verge of stall. For all higher α, the increased size of the separation bubble indicates that the flow is unable to reattach, in accordance with the lift curve (Figure 4). This is typical for thin airfoil stall, where a separation bubble separating at the leading edge is unable to reattach. The same type of stall was observed by Bragg et al.[11] for their horn icing geometry. Thus, the mean flow fields qualitatively agree with earlier reported results for all contamination geometries.

The drag (Figure 4) increases with increasing size of the separation bubble for type C contamination. The separation bubble leads to high drag also for low and negative α. For the other contamination geometries, the increase in drag is largest compared to the clean airfoil when separation is visible in the FoV. Thus, separation is the most important factor for the increase in drag.

For interested readers, the mean velocity components are available as supplementary material to this article Supporting Information. These are open to others for comparisons, validation of CFD-results and other applications.

3.2 | Turbulent kinetic energy

The TKE was calculated as

$$TKE = \frac{1}{2}\left(\langle u^2 \rangle + \langle v^2 \rangle\right),$$ (1)

which is a two-dimensional surrogate. Figure 6 shows TKE of the different cases. The figure suggests that most of the TKE is associated with flow separation. For both type A and B contamination geometries, the TKE is highest for $\alpha = 16°$, which is above α_{stall}. The turbulent region starts at the leading edge, in contrast to the clean case, where the turbulent region starts farther downstream. This is in agreement with the mean flow fields, as the separation happens farther downstream in the absence of contamination. At $\alpha = 14°$, there is a higher level of TKE near the leading edge, before it decreases in magnitude farther downstream. This, combined with the mean velocity fields, suggests that the flow separates before it reattaches, and the airfoil has not reached α_{stall}.

Focusing on the type B contamination for $4° \leq \alpha \leq 10°$, there is TKE located above the contamination. This is an indication that the presence of the contamination leads to turbulent transition of the boundary layer at the leading edge. Bragg et al.[8] state that the surface roughness of icing usually is higher than the local boundary layer, which leads to turbulent transition. This is also the reason why the separation point moves upstream on the airfoil for the streamwise contaminations. At $\alpha = 14°$, type B contamination also results in turbulent flow over the entire airfoil. However, the lift curve and mean flow field do not show full separation. Thus, the increased level of turbulence generated over the contamination keeps the flow attached to the surface, as indicated in Section 3.1.

For type C contamination, the highest turbulence levels are found in the shear layer between the reverse flow inside the separation bubble and the freestream flow. The turbulent shear layer is thin close to the horn and grows wider farther downstream. When $\alpha = 6°$, the turbulent shear layer reaches the airfoil surface within the FoV, indicating that the flow reattaches for this particular case. For lower α, the shear layer quickly reaches the airfoil, indicating reattachment. These observations agree with those made from the mean flow field. The high turbulence region is wide when it reaches the airfoil for all the mentioned cases, suggesting that the point where the flow reattaches to the airfoil is fluctuating upstream and downstream on the surface, thus making it unstable. The fluctuations and the shape of the shear layer are in agreement with several earlier publications on the separation bubble downstream of horn icing.[27,28]

For type C contamination, the region of high TKE is wider in the $\alpha = 10°$ case than for any of the other α. This suggests that the height of the separating shear layer is more intermittent for this case; that is, the distance from the airfoil to the separating shear layer is varying more. To investigate the intermittency further, the height of the shear layer must be defined. For this purpose, the longest continuous contour for a certain velocity threshold was found. This was done in a specified interrogation window given by $0.1 \leq x/c \leq 0.4$ and $0.1 \leq y/c \leq 0.4$. For every x-position, the contour might have several values. Therefore, the point on this contour located farthest from the airfoil, at a given x-location, was defined as the height of the separation layer. The probability distribution P for each x-position was calculated and is shown in Figure 7 for the four highest α. A velocity threshold of $U_{tot} = 0.8U_\infty$ was used. The black contours in the figure illustrate the edge of the probability distribution, where the edge is defined as the point where the value of the distribution is $P_{edge} = 0.02$. Figure 8 shows the width of the probability distribution, measured in the flow coordinate system. The width of the probability distribution is larger for $\alpha = 10°$ than for the $14°$ and $16°$ cases. In fact, it is between 20% and 25% wider for $\alpha = 10°$, depending on the downstream position. Thus, the flow is more intermittent for this case. For $\alpha = 6°$, the width of the probability distribution is smaller than for the fully separated flows at higher α, and the flow is less intermittent. Note that results are only shown for one velocity threshold and one distribution threshold. However, the same calculations were performed for different thresholds, and similar results were achieved for all tested values. The higher level of intermittency might lead to vibrations in the airfoil and is thus important for the loads acting on a turbine. As $\alpha = 10°$ is within the normal operation region, it is important to understand the physics of the flow acting on the airfoil in this situation.
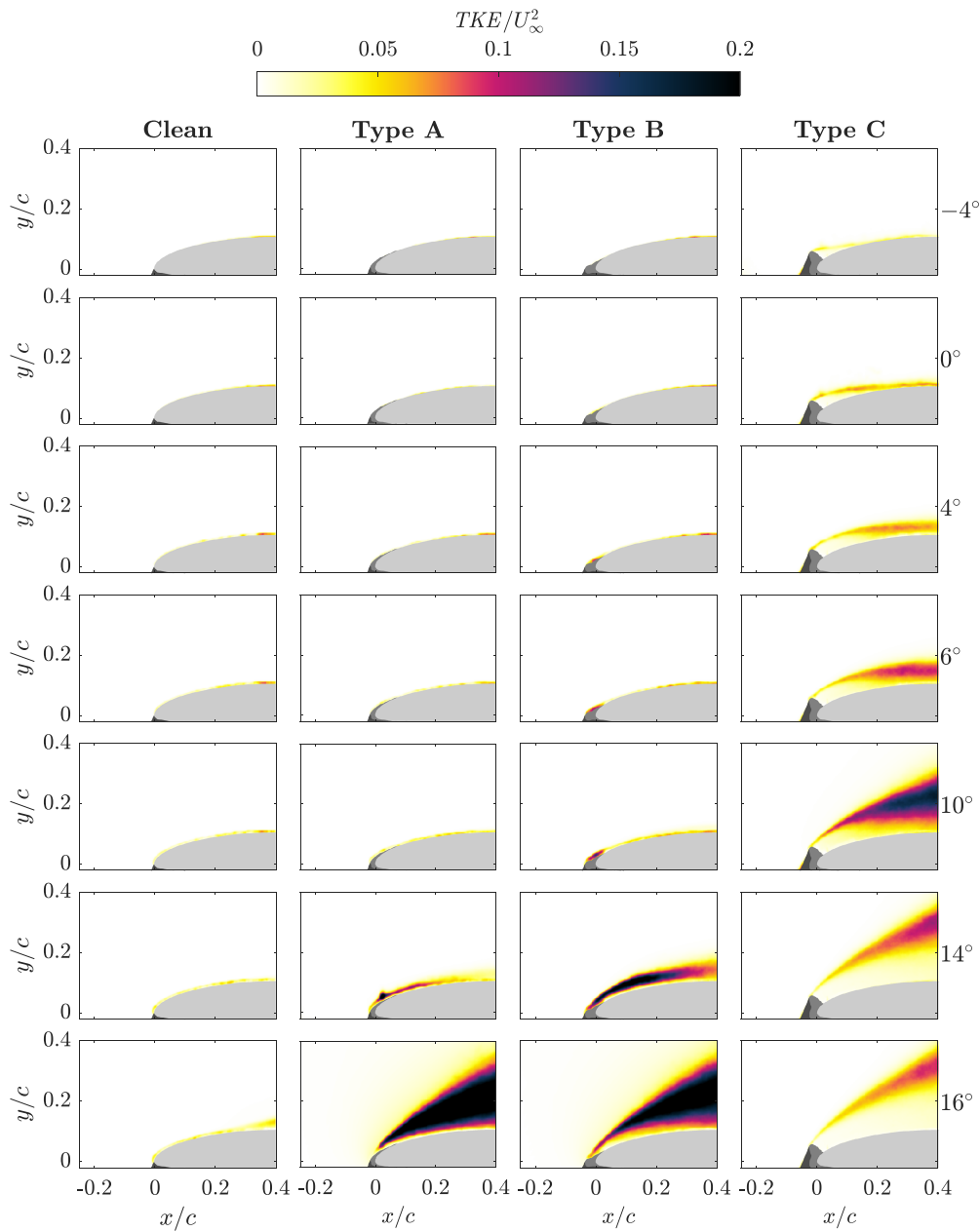
FIGURE 6 Two-dimensional turbulent kinetic energy surrogate for all experimental cases, normalised by the freestream velocity [Colour figure can be viewed at wileyonlinelibrary.com]

3.3 | Vorticity

The out of plane vorticity, defined as

$$\omega_z = \frac{\partial v}{\partial x} - \frac{\partial u}{\partial y},$$ (2)

is a measure of the local spinning motion in the flow. The mean vorticity for all cases is presented in Figure 9. The sign convention used herein means the vorticity is clockwise (blue) near the suction side of the airfoil for all regions where recirculation does not occur. This is a result of the boundary layer, where the velocity increases with increasing distance from the airfoil. When the flow has separated, the flow close to the airfoil surface is opposite in direction, and the boundary layer gives counter-clockwise vorticity.
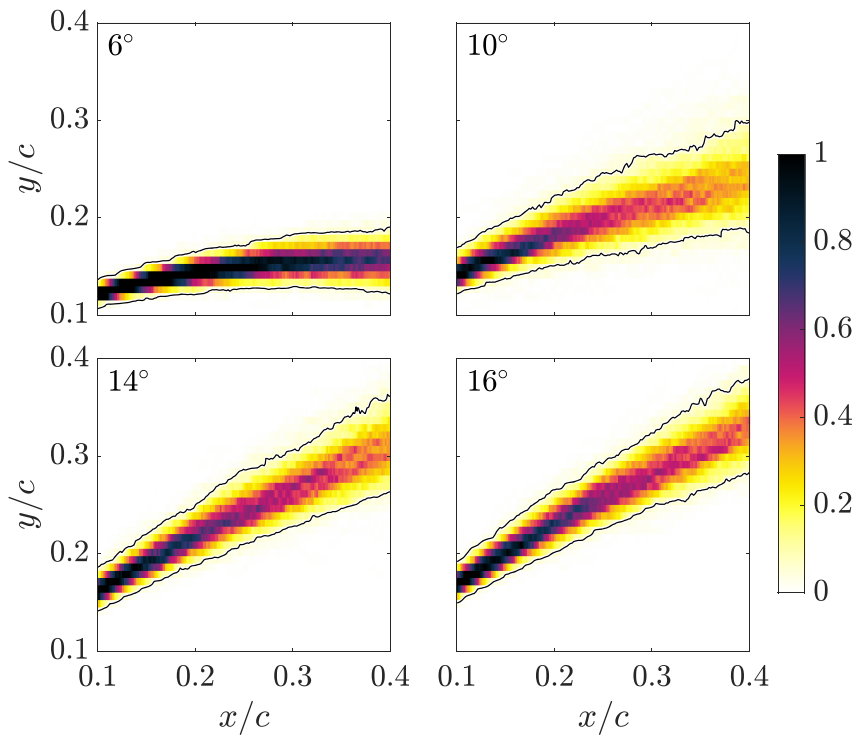
FIGURE 7 Probability distribution of the height of the separated flow, found at a threshold where $U_{tot} = 0.8U_\infty$, for the flow behind the type C contamination. Black lines indicate where the value is $P_{edge} = 0.02$ [Colour figure can be viewed at wileyonlinelibrary.com]
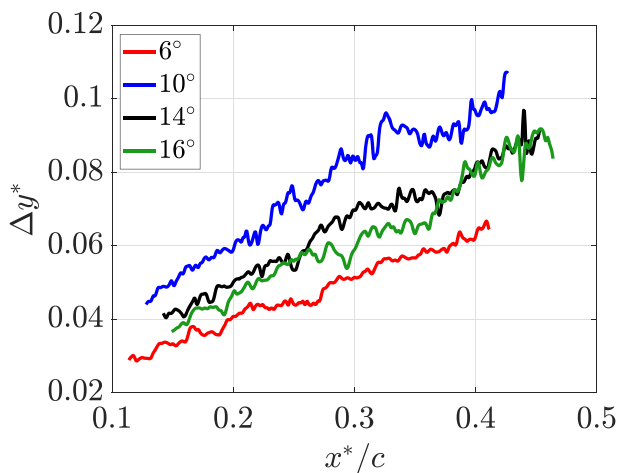

FIGURE 8 Width of the probability distribution in Figure 7 with a threshold value of $P_{edge} = 0.02$ [Colour figure can be viewed at wileyonlinelibrary.com]

For the type B contamination, at $\alpha = 14°$, a small region of weak counter-clockwise vorticity is present close to the airfoil surface. This indicates a thin recirculating region and thus separated flow. The high level of vorticity just over the surface of the airfoil, for $x/c \geq 0.2$, shows that the flow reattaches, and that stall has not been reached at this α. This agrees with the discussion in Section 3.2, which concluded that the flow was not fully separated for this case. The streamwise horn acts more like a regular horn geometry at high α, as the flow separates at the leading edge. The separation bubble increases the drag relative to the clean case. The lift of the airfoil is not reduced by the phenomena. In fact, this is the only region where the C_l (Figure 4) for any of the contamination geometries is as large as for the for the clean case.

For the cases where the flow separates, the vorticity is high in and around the shear layers described earlier. These are the same regions as where the turbulent energy is highest. The mean vorticity is clockwise in these regions, showing that the main vortices coming from the separation point rotate clockwise. The layer of clockwise mean vorticity is larger for $\alpha = 10°$ than higher α for the type C contamination. This indicates that the distance from the airfoil to the layer of high vorticity, corresponding to the shear layer, is varying in the instantaneous fields. This agrees with what was observed for the *TKE* in Figure 6. It is also evident that the magnitude of the clockwise mean vorticity is higher for the separated flows which reattach, than for the flows that do not reattach. This can be associated with the thinner shear layer in these flows, which gives larger velocity gradients.

For type C contamination, clockwise vorticity is also observed for a small region just downstream of the horn, close to the airfoil surface. The region is small and may be noise rather than actual measurements. However, the observation is in agreement with the second, smaller, recirculation zone reported earlier by Jacobs and Bragg.[27] It was not possible to identify this region in the velocity fields obtained; thus, the second
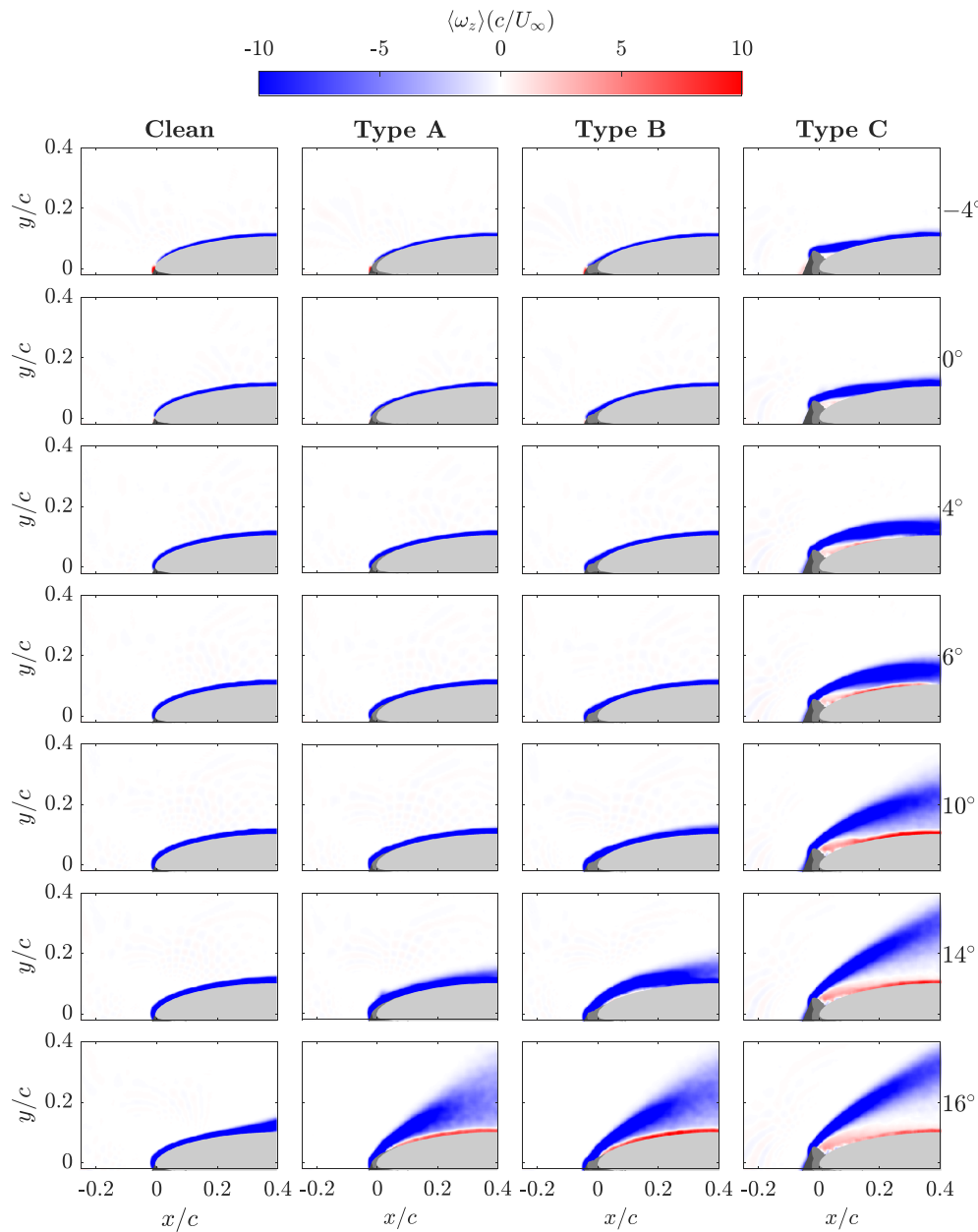
FIGURE 9 Normalised mean vorticity for all experimental cases [Colour figure can be viewed at wileyonlinelibrary.com]

bubble is either very small or not present in the current flow. The discrepancy might arise due to differences in the experimental setups. Jacobs and Bragg[27] used a different airfoil (NACA0012), a different contamination geometry and a higher Re ($Re_c = 9 \times 10^5$); thus, the specific features of their flow fields and the ones presented herein may not be directly comparable.

4 | PROPER ORTHOGONAL DECOMPOSITION

Snapshot POD, developed by Sirovich,[48] was used to find the spatial modes of the flow. The computations were performed in the same manner as by Meyer et al.[49,50] POD separates the flow into a certain number of modes. Each mode, $\boldsymbol{\phi}^i$, represents some repeating structure of the flow. The eigenvalue λ_i represents the relative energy content of the corresponding mode. Therefore, POD gives information about structures of the flow and how dominating they are in energy content. Note that the magnitude and sign of values in each mode do not have physical meanings in themselves. Only when they are combined with reconstruction coefficients a_i can they be used to reproduce the instantaneous flow fields, also called snapshots, $\mathbf{u}^n$. The equation

$$\mathbf{u}^n = \sum_{i=1}^{N} a_i^n \boldsymbol{\phi}^i \tag{3}$$

relates the instantaneous velocity fields to the reconstruction coefficients and POD modes.[48] Here, the superscript n refers to number of the snapshot, and i refers to the number of the mode. The POD analysis was performed with the mean velocity subtracted from the instantaneous velocity fields, leaving the mean velocity as the zeroth mode.

4.1 | Energy of modes

Figure 10 displays the cumulative energy fraction of the modes for the fluctuating velocity components at all α and contamination geometries. The modes are sorted by the magnitude of λ, such that the most energetic mode is the first mode. Note that the modes only represent the fluctuations of the flow. If the mean flow field had been included in the calculation of the modes, the first mode would have represented the mean flow and carried a large portion of the energy. For cases without separation, the first modes carry a low portion of the total fluctuating energy. It thus follows that the clean case has no fluctuating modes with particularly high energy. For cases with visible separation, the first modes contain a larger portion of the energy. From mode 100 to 1000, only small differences are seen between the cumulative energy curves, for all cases, suggesting that these modes do not contain case specific physics.

For type A and B contaminations, the first few modes contain a larger portion of the fluctuating energy of the flow when $\alpha = 16°$. This suggests that periodic structures are present in these flow fields and that a few of these structures contain most of the fluctuating energy. The cumulative energy curves for $\alpha = 16°$ for both mentioned cases look similar, which suggests that the flow fields are similar. This is discussed in greater detail in Section 4.2. It is also interesting to note that, for both type A and B contaminations, the cases with $\alpha = -4°$ have a slightly higher relative energy content in the first mode than cases $0° \le \alpha \le 14°$. The present experimental setup is not suited to give a full explanation of this. However, the observation suggests that periodic structures are present on the pressure side of the airfoil and that a small portion of them is visible upstream of the airfoil. At this α, the drag of the contaminated airfoil increases (see Figure 4). As increased drag is associated with flow separation (Section 3.1) and coherent structures, this supports the observation.

For type C contamination, the first modes have higher energy content for $\alpha = 6°$ compared to lower α. The highest energy modes are found for $\alpha = 10°$. For the two highest α, the energy content of the first modes decreases compared to $\alpha = 10°$. As high energy modes are an indication of coherent structures in the flow, this identifies that there is more periodicity in the flow at $\alpha = 10°$ than for both higher and lower α. This is in agreement with the analysis shown in Section. 3.2. For all cases with high energy modes, only the first few contain more fluctuating energy than the corresponding modes for the other cases. There are thus only a few repeating structures that carry a larger share of the flow energy.
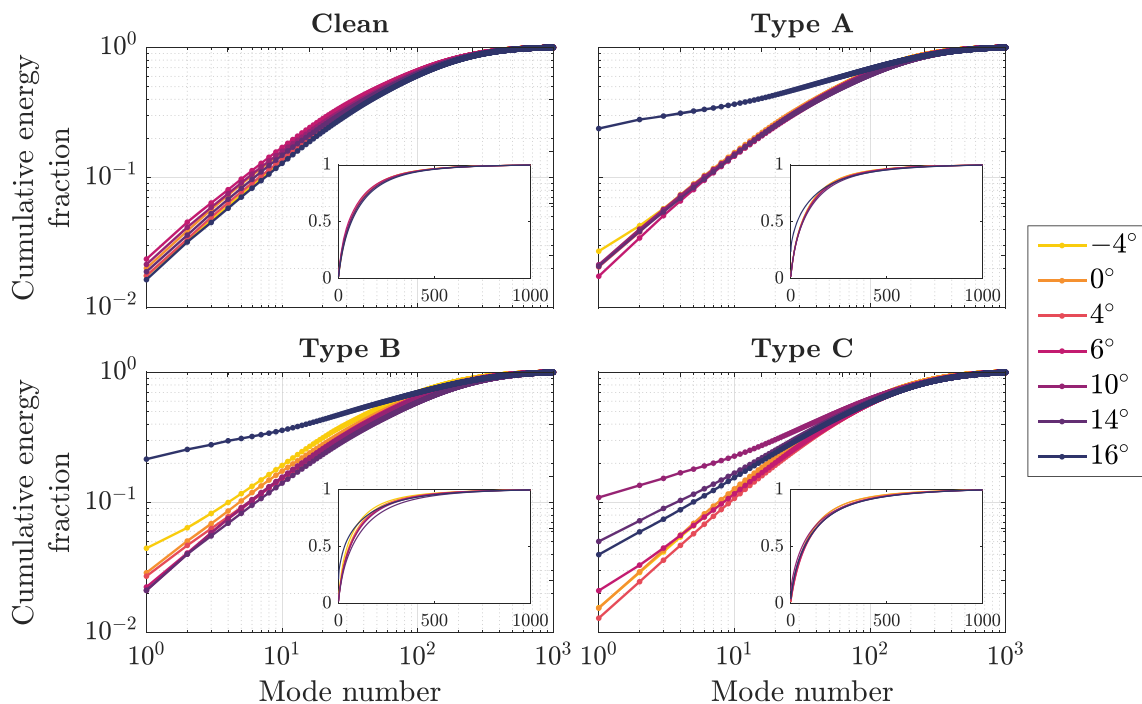

FIGURE 10 Cumulative energy fraction of the POD modes. The insets show the same information in linear scale [Colour figure can be viewed at wileyonlinelibrary.com]

FIGURE 11 Number of modes needed to capture 40% of the energy of the fluctuations in the flow [Colour figure can be viewed at wileyonlinelibrary.com]
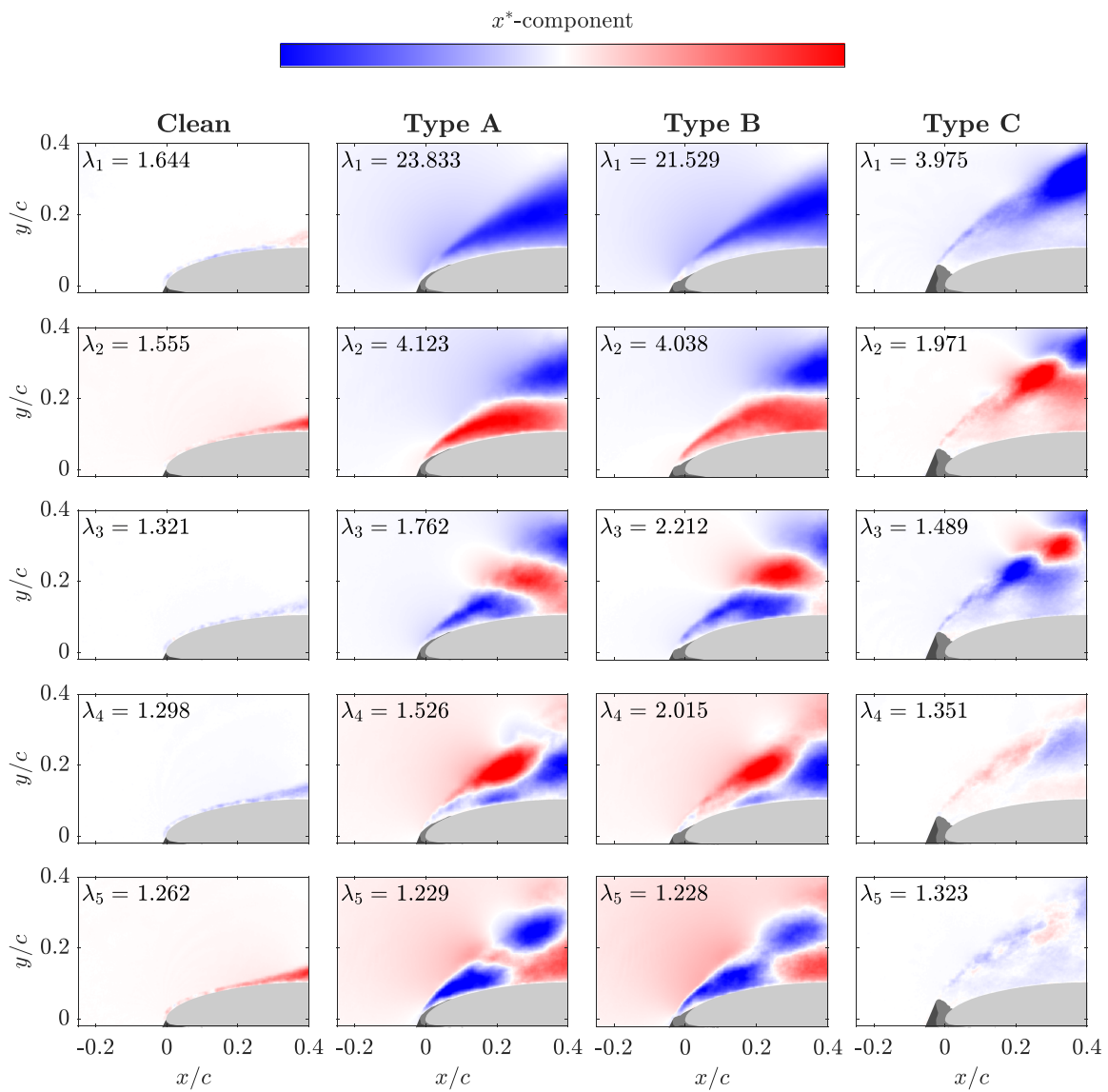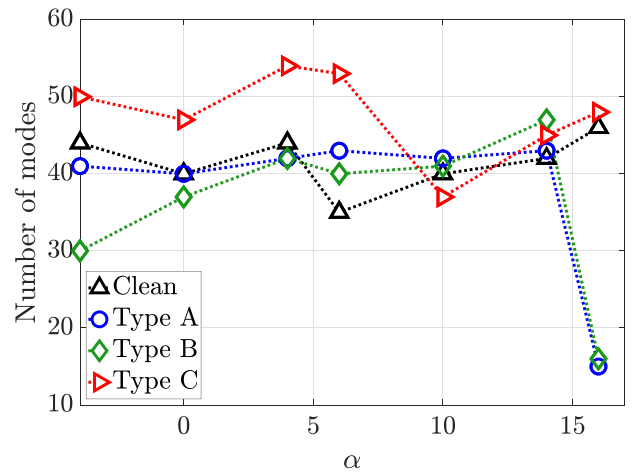

FIGURE 12 Five first x^*-direction velocity modes for α = 16°, for all contamination geometries and the clean airfoil [Colour figure can be viewed at wileyonlinelibrary.com]

To get an impression of the number of modes required to model the flow, it is instructive to see how many modes are needed to represent some degree of the fluctuating energy of the flow. Here, we choose 40% of the energy as a point for comparison, which is arbitrary, but the results do not significantly change with the choice of a different threshold. Choosing a too high fraction would lead to experimental noise possibly being part of the modelling, which is not desirable.[51] Figure 11 shows the number of modes necessary to represent the chosen energy fraction. For type A and B contamination at $\alpha = 16°$, approximately 15 modes are sufficient, in contrast to all other cases. The sharp drop in the number of modes indicates that the separated flow for these cases is dominated by coherent motions, while such features are less important in the flow at lower α. It is also interesting that the type C contamination cases, at $-4° \leq \alpha \leq 6°$, need more modes to be modelled. This suggests that the flow inside the recirculation bubble is not dominated by any coherent or repeating structure when it reattaches to the airfoil. Instead, many different structures carry smaller portions of the energy. At higher α, a larger number of modes are needed to reconstruct the flow, indicating fewer dominating coherent motions. Even though there are variations between the cases, the maximum number of modes needed to reach 40% of the energy does not exceed 54. Thus, there is a potential for using ROM to predict the flow over contaminated airfoils while still capturing the significant flow physics.

4.2 | POD modes for $\alpha = 16°$

As the low order modes represent the energy carrying structures of the flow, it is instructive to study examples of them. The first five POD modes for the fluctuating velocity components at $\alpha = 16°$, for all contamination cases, are shown in Figures 12 (x^*-component) and 13 (y^*-component).
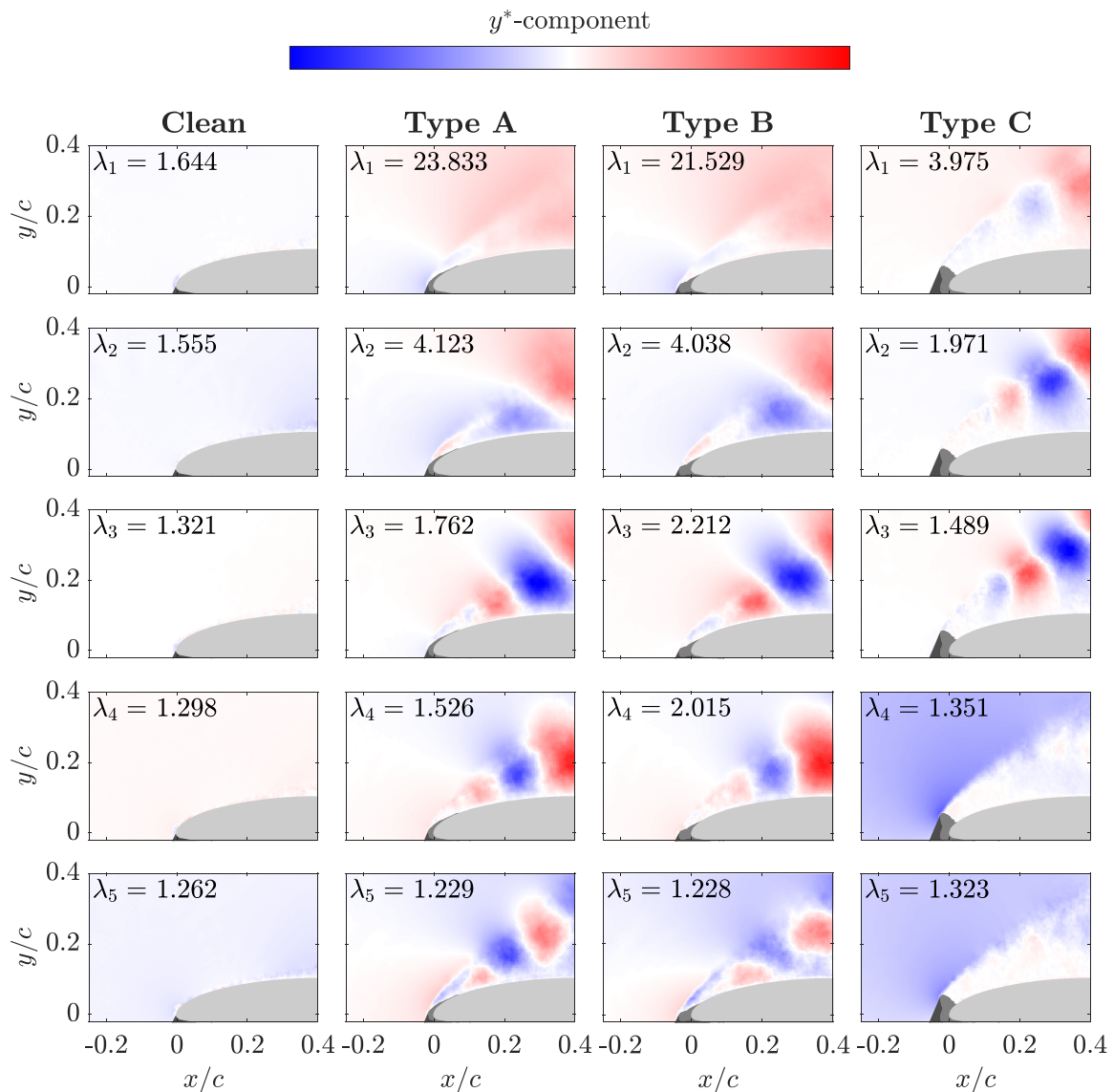

FIGURE 13 Five first y^*-direction velocity modes for $\alpha = 16°$, for all contamination geometries and the clean airfoil [Colour figure can be viewed at wileyonlinelibrary.com]

Only small fluctuations close to the airfoil are present for the case without contamination. For type A and B contaminations, the first five modes show similar behaviour, both for the x^*-component and the y^*-component. This represents more than 30% of the fluctuating energy for both cases. Thus, the dominating structures of the flow are similar for the two streamwise contamination geometries. For the stalled situation, the major structures of the flow field are determined by the large features of the contamination geometry. There is a decreasing trend in the size of the structures from the first to the fifth mode. This trend is visible for all contamination geometries. As one might expect, the largest structures carry the largest portions of the fluctuating energy. It is also interesting that the fourth and fifth modes in the y^*-direction, for type C contamination, do not include structures in the separated flow. Instead, these modes show variations in the vertical velocity component in the high velocity flow outside the separation layer.

5 | CONCLUSION

PIV measurements were performed on an NREL S826 reference airfoil with different leading-edge contaminations. Three different icing-inspired contamination geometries were used, and the clean case was also investigated as a reference. Experiments were performed for $-4° \leq \alpha \leq 16°$ at $Re_c = 4.55 \times 10^5$, which is within the Re-independent regime of the airfoil.

Mean velocity fields show a separation bubble behind the horn of the type C contamination, which grows in size with increasing α. The turbulent kinetic energy is high in the shear layer separating the recirculating region from the inviscid flow. For $\alpha = 10°$, the shear layer is unstable and instantaneously varies over a wide range of positions.

For the streamlined contamination geometries (type A and B), separation is visible in the mean flow fields for $\alpha \geq 14°$ and occurs close to or at the leading edge. This means separation happens farther upstream on the airfoil than for the clean case. The turbulent kinetic energy is high over the entire recirculating region and the shear layer when the flow is separated. Recirculation, and thus separation, is found for type B contamination at $\alpha = 14°$, but the flow is able to reattach in most snapshots. This is in agreement with the lift curve, which shows that this α is on the verge of stall for type B contamination. At the same α, type A contamination does not lead to a permanent separation bubble, but the high level of turbulent kinetic energy suggests the flow is separating intermittently.

POD demonstrated that the flow can be described by fewer modes when it has separated. For such cases, reconstruction of the main properties of the flow field is possible from a limited number of modes. This means that it is possible to model the flow based on a reduced number of modes with POD, which is promising for those in the community who seek to exploit this avenue for rapid or real-time simulations.

This study has focused on 2-D analogues of leading-edge contamination on a wind turbine airfoil. These 2-D contamination profiles were inspired by icing geometries, which are by their very nature 3D (e.g., previous studies[9,26]). The approach taken here was to use profiles that were surrogates for the average of the contamination profile along the length and use this in a single plane. Future studies should investigate 3-D contamination profiles in multiple planes and average them across the span to see if bulk flow characteristics can be identified. While the focus in the future should progress towards 3-D geometries, the data set presented here nonetheless provides significant insight on the local mechanisms that drive the flow features and total forces on an iced airfoil, providing clear phenomenological backing for the previously reported lift and drag behaviour. The present results may also be useful as a reference for future modellers who seek to simulate flows of this nature, although one must consider the experimental set-up when attempting to replicate the results.

ORCID
Magnus K. Vinnes https://orcid.org/0000-0003-0980-1827
R. Jason Hearst https://orcid.org/0000-0003-2002-8644

REFERENCES
1. Renewables 2019 global status. Report. tech. rep., REN21; 2019. https://www.ren21.net/gsr-2019. Accessed June 16, 2020.
2. Han W, Kim J, Kim B. Effects of contamination and erosion at the leading edge of blade tip airfoils on the annual energy production of wind turbines. *Renew Energy*. 2018;115:817-823. https://doi.org/10.1016/j.renene.2017.09.002
3. Dollinger C, Balaresque N, Gaudern N, Gleichauf D, Sorg M, Fischer A. IR thermographic flow visualization for the quantification of boundary layer flow disturbances due to the leading edge condition. *Renew Energ*. 2019;138:709-721. https://doi.org/10.1016/j.renene.2019.01.116
4. Botta G, Cavaliere M, Holttinen H. Ice accretion at Acqua Spruzza and its effects on wind turbine operation and loss of energy production. In: Proceedings of BOREAS IV; 1998; Enontekiö, Finland.

5. Han Y, Palacios J, Schmitz S. Scaled ice accretion experiments on a rotating wind turbine blade. *J Wind Eng Ind Aerod*. 2012;109:55-67. https://doi.org/10.1016/j.jweia.2012.06.001

6. Yirtici O, Ozgen S, Tuncer IH. Predictions of ice formations on wind turbine blades and power production losses due to icing. *Wind Energy*. 2019;22(7): 945-958. https://doi.org/10.1002/we.2333

7. Parent O, Ilinca A. Anti-icing and de-icing techniques for wind turbines: Critical review. *Cold Reg Sci and Technol*. 2011;65(1):88-96. https://doi.org/10.1016/j.coldregions.2010.01.005

8. Bragg M, Broeren A, Addy H, Potapczuk M, Guffond D, Montreuil E. Airfoil ice-accretion aerodynamic simulation. In: 45th AIAA Aerospace Sciences Meeting and Exhibit; 2007; Reno, Nevada.

9. Gao L, Liu Y, Hu H. An experimental investigation of dynamic ice accretion process on a wind turbine airfoil model considering various icing conditions. *Int J Heat Mass Tran*. 2019;133:930-939. https://doi.org/10.1016/j.ijheatmasstransfer.2018.12.181

10. Han Y, Palacios J. Airfoil-performance-degradation prediction based on nondimensional icing parameters. *AIAA J*. 2013;51(11):2570-2581. https://doi.org/10.2514/1.J052207

11. Bragg MB, Broeren AP, Blumenthal LA. Iced-airfoil aerodynamics. *Prog Aerosp Sci*. 2005;41(5):323-362. https://doi.org/10.1016/j.paerosci.2005.07.001

12. McCullough GB, Gault DE. Examples of three representative types of airfoil-section stall at low speed, NACA Technical Note 2502; 1951. https://ntrs.nasa.gov/archive/nasa/casi.ntrs.nasa.gov/19930083422.pdf. Accessed June 16, 2020.

13. Tani I. Low-speed flows involving bubble separations. *Prog Aerosp Sci*. 1964;5:70-103. https://10.1016/0376-0421(64)90004-1

14. Anderson J. *Fundamentals of Aerodynamics*. 6th ed. New York: McGraw-Hill Education; 2017.

15. De Gregorio F, Ragni A, Airoldi M, Romano GP. PIV investigation on airfoil with ice accretions and resulting performance degradation. In: ICIASF 2001 Record, 19th International Congress on Instrumentation in Aerospace Simulation Facilities (Cat. No.01CH37215); 2001; Cleveland, Ohio.

16. Etemaddar M, Hansen MOL, Moan T. Wind turbine aerodynamic response under atmospheric icing conditions. *Wind Energy*. 2014;17(2):241-265. https://doi.org/10.1002/we.1573

17. Blasco P, Palacios J, Schmitz S. Effect of icing roughness on wind turbine power production. *Wind Energy*. 2017;20(4):601-617. https://doi.org/10.1002/we.2026

18. Krøgenes J, Brandrud L. Aerodynamic performance of the NREL S826 airfoil in icing conditions. *Master thesis*: NTNU; 2017. https://ntnuopen.ntnu.no/ntnu-xmlui/handle/11250/2454897. Accessed June 16, 2020.

19. Gao L, Liu Y, Zhou W, Hu H. An experimental study on the aerodynamic performance degradation of a wind turbine blade model induced by ice accretion process. *Renew Energ*. 2019;133:663-675. https://doi.org/10.1016/j.renene.2018.10.032

20. Hann R, Hearst RJ, Sætran LR, Bracchi T. Experimental and numerical icing penalties of an S826 airfoil at low reynolds numbers. *Aerospace*. 2020;7(4): 46. https://doi.org/10.3390/aerospace7040046

21. Pouryoussefi SG, Mirzaei M, Nazemi M-M, Fouladi M, Doostmahmoudi A. Experimental study of ice accretion effects on aerodynamic performance of an NACA 23012 airfoil. *Chinese J Aeronaut*. 2016;29(3):585-595. https://doi.org/10.1016/j.cja.2016.03.002

22. Vinnes MK, Li L, Hearst RJ. PIV of the flow over a NREL S826 airfoil subjected to different ice accretions. In: Örlü R, Talamelli A, Peinke J, Oberlack M, eds. *Progress in Turbulence VIII*. Springer Proceedings in Physics. Vol. 226. Springer, Cham; 2019:331-336. https://doi.org/10.1007/978-3-030-22196-6_52

23. Xiao M, Zhang Y, Zhou F. Numerical study of iced airfoils with horn features using large-eddy simulation. *J Aircraft*. 2019;56(1):94-107. https://doi.org/10.2514/1.C034986

24. Gray VH, von Glahn UH. Aerodynamic effects caused by icing of an unswept NACA 65A004 airfoil, National Advisory Commitee for Aeronautics; 1958. https://ntrs.nasa.gov/archive/nasa/casi.ntrs.nasa.gov/19810068589.pdf. Accessed June 16, 2020.

25. Jasinski WJ, Noe SC, Selig MS, Bragg MB. Wind turbine performance under icing conditions. *J Sol Energ*. 1998;120(1):60-65. https://doi.org/10.1115/1.2888048

26. Liu Y, Li L, Chen W, Tian W, Hu H. An experimental study on the aerodynamic performance degradation of a uas propeller model induced by ice accretion process. *Exp Therm Fluid Sci*. 2019;102:101-112. https://doi.org/10.1016/j.expthermflusci.2018.11.008

27. Jacobs J, Bragg M. Particle image velocimetry measurements of the separation bubble on an iced airfoil. In: 24th AIAA Applied Aerodynamics Conference; 2006; San Francisco, California.

28. Jacobs J, Bragg M. Two- and three-dimensional iced airfoil separation bubble measurements by particle image velocimetry. In: 45th AIAA Aerospace Sciences Meeting and Exhibit; 2007; Reno, Nevada.

29. Kiya M, Sasaki K. Structure of large-scale vortices and unsteady reverse flow in the reattaching zone of a turbulent separation bubble. *J Fluid Mech*. 1985;154:463-491. https://doi.org/10.1017/S0022112085001628

30. Spazzini PG, Iuso G, Onorato M, Zurlo N, Di Cicca GM. Unsteady behavior of back-facing step flow. *Exp Fluids*. 2001;30(5):551-561. https://doi.org/10.1007/s003480000234

31. Ansell PJ, Bragg MB. Measurement of unsteady flow reattachment on an airfoil with an ice shape. *AIAA J*. 2014;52(3):656-659. https://doi.org/10.2514/1.J052519

32. Mirzaei M, Ardekani MA, Doosttalab M. Numerical and experimental study of flow field characteristics of an iced airfoil. *Aerosp Sci Technol*. 2009;13 (6):267-276. https://doi.org/10.1016/j.ast.2009.05.002

33. Siddiqui MS, Fonn E, Kvamsdal T, Rasheed A. Finite-volume high-fidelity simulation combined with finite-element-based reduced-order modeling of incompressible flow problems. *Energies*. 2019;12(7):1271. https://doi.org/10.3390/en12071271

34. Lengani D, Simoni D, Ubaldi M, Zunino P. POD analysis of the unsteady behavior of a laminar separation bubble. *Exp Therm Fluid Sci*. 2014;58:70-79. https://doi.org/10.1016/j.expthermflusci.2014.06.012

35. Mohan AT, Gaitonde DV, Visbal MR. Model reduction and analysis of deep dynamic stall on a plunging airfoil. *Comput Fluids*. 2016;129:1-19. https://doi.org/10.1016/j.compfluid.2016.01.017

36. Traphan D, Wester TTB, Peinke J, Gülker G. On the aerodynamic behavior of an airfoil under tailored turbulent inflow conditions. In: 5th International Conference on Experimental Fluid Mechanics; 2018; Munich, Germany.

37. Zhao M, Zhao Y, Liu Z, Du J. Proper orthogonal decomposition analysis of flow characteristics of an airfoil with leading edge protuberances. *AIAA J*. 2019;57(7):2710-2721. https://doi.org/10.2514/1.J058010

38. Somers DM. The S825 and S826 airfoils. *tech. rep.*, NREL; 2005. https://wind.nrel.gov/airfoils/Documents/S825,_S826_Design.pdf. Accessed June 16, 2020.

39. Sarlak H, Mikkelsen R, Sarmast S, Sørensen JN. Aerodynamic behaviour of NREL S826 airfoil at Re=100,000. *J Phys Conf Ser*. 2014;524:12027. https://doi.org/10.1088/1742-6596/524/1/012027

40. Sarlak H, Frère A, Mikkelsen R, Sørensen JN. Experimental investigation of static stall hysteresis and 3-dimensional flow structures for an nrel s826 wing section of finite span. *Energies*. 2018;11(6):1418. https://doi.org/10.3390/en11061418

41. Bartl J, Sagmo KF, Bracchi T, Sætran L. Performance of the NREL S826 airfoil at low to moderate Reynolds numbers—a reference experiment for CFD models. *Eur J Mech B-Fluid*. 2019;75:180-192. https://doi.org/10.1016/j.euromechflu.2018.10.002

42. Wright W. User's manual for LEWICE version 3.2. *tech. rep.*, NASA; 2008. https://ntrs.nasa.gov/archive/nasa/casi.ntrs.nasa.gov/20080048307.pdf. Accessed June 16, 2020.

43. Wright W, Rutkowski A. Validation results for LEWICE 2.0. *tech. rep.*, NASA; 1999. https://ntrs.nasa.gov/archive/nasa/casi.ntrs.nasa.gov/19990021235.pdf. Accessed June 16, 2020.

44. Wright W. Validation results for LEWICE 3.0. *tech. rep.*, NASA; 2005. https://ntrs.nasa.gov/archive/nasa/casi.ntrs.nasa.gov/20050160961.pdf. Accessed June 16, 2020.

45. Wieneke B. PIV uncertainty quantification from correlation statistics. *Meas Sci Technol*. 2015;26(7):74002. https://doi.org/10.1088/09570233/26/7/074002

46. Neal DR, Sciacchitano A, Smith BL, Scarano F. Collaborative framework for PIV uncertainty quantification: the experimental database. *Meas Sci Technol*. 2015;26(7):74003. https://doi.org/10.1088/0957-0233/26/7/074003

47. Sciacchitano A, Neal DR, Smith BL, Warner SO, Vlachos PP, Wieneke B, Scarano F. Collaborative framework for PIV uncertainty quantification: comparative assessment of methods. *Meas Sci Technol*. 2015;26(7):74004. https://doi.org/10.1088/0957-0233/26/7/074004

48. Sirowich L. Turbulence and the dynamics of coherent structures, Part 1: Coherent structures. *Q Appl Math*. 1987;45(3):561-571. https://doi.org/10.1090/qam/910462

49. Meyer KE, Pedersen JM, Özcan O. A turbulent jet in crossflow analysed with proper orthogonal decomposition. *J Fluid Mechanics*. 2007;583:199-227. https://doi.org/10.1017/S0022112007006143

50. Meyer KE, Cavar D, Pedersen JM. POD as tool for comparison of PIV and LES data. In: Proceedings of 7th International Symposium on Particle Image Velocimetry; 2007; Rome, Italy.

51. van der Kindere J, Ganapathisubramani B. Effect of length of two-dimensional obstacles on characteristics of separation and reattachment. *J Wind Eng Ind Aerod*. 2018;178:38-48. https://doi.org/10.1016/j.jweia.2018.04.018

SUPPORTING INFORMATION

Additional supporting information may be found online in the Supporting Information section at the end of this article.